International Journal of Multiphase Flow 181 (2024) 105021

Contents lists available at ScienceDirect

International Journal of Multiphase Flow

journal homepage: www.elsevier.com/locate/ijmulflow

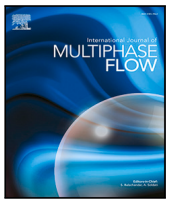

# Machine learning-enhanced PIV for analyzing microfiber-wall turbulence interactions

Vlad Giurgiu [a], Leonel Beckedorff [a], Giuseppe C.A. Caridi [a], Christian Lagemann [b], Alfredo Soldati [a,c,*]

[a] Institute of Fluid Mechanics and Heat Transfer, TU Wien, 1060 Wien, Austria
[b] AI Institute in Dynamic Systems, University of Washington, 98195 Seattle, USA
[c] Polytechnic Department, University of Udine, 33100 Udine, Italy

ARTICLE INFO

*Keywords:*
Machine learning
PIV
Wall turbulence
Channel flow
Microplastic
Fiber
Rotation rate
Hairpin vortex

ABSTRACT

A machine learning-based approach, RAFT-PIV, is used to measure with single-pixel resolution the flow field around a microplastic fiber in a turbulent channel flow at a Shear Reynolds number of 1000. The results reveal the interaction of the fiber with a hairpin vortex. The fiber rotation rate is correlated with slip velocity distributions along the fiber length, demonstrating higher rotation rates with increased slip velocity gradients. The fiber's alignment with the spanwise direction during its trajectory is explained through its progressive alignment with the head of a hairpin vortex, characterized by the swirling strength, shear strain rate, and local flow velocity. Higher fiber rotation rates were found likelier in the presence of a vortical structure. These findings highlight the potential of machine learning-enhanced PIV techniques to deepen our understanding of fiber-turbulence interactions, essential for applications such as microplastic pollution mitigation.

## 1. Introduction

Understanding the dynamics of microscopic fibers in turbulent flows is crucial for various environmental and industrial applications, including pollution control, marine biology, and chemical engineering (Voth and Soldati, 2017). The anisotropy of these particles leads to orientation-dependent drag coefficients, resulting in a resistance tensor which promotes more complex modes of solid-body rotation in comparison with spherical particle (Voth and Soldati, 2017).

In the specific case of oceanic pollution, microplastics have a size of about one millimetre, a length-to-diameter aspect ratio of about 100, and their dynamics depend on the forces and torques applied by the smallest turbulence scales. Since no closed form of the drag on non-spherical particles is currently available, the prediction of the dynamics of anisotropic particles and in turn of their sedimentation and dispersion rates remains beyond current possibilities. To find such detailed information field measurements are out of question, with controlled experimental campaigns remaining the only viable option. In previous works, we have described a channel facility in which controlled and reproducible wall turbulence can be realized (Giurgiu et al., 2023), and the optical techniques by which we can measure the dynamics of quasi-inertialess high aspect ratio fibers longer than few tens Kolmogorov length scales (Alipour et al., 2021; Giurgiu et al., 2024). However, to model fiber dynamics in turbulence it is necessary to measure simultaneously fiber motion and the motion of the surrounding fluid. This study uses a machine learning approach to achieve precise (i.e., single-pixel resolution) flow prediction around a fiber with higher resolution than the traditional cross-correlation-based Particle Image Velocimetry (CC-PIV) technique.

CC-PIV has been widely used to measure velocity fields in fluid flows. The procedure involves seeding the fluid with tracing particles, which are illuminated and imaged with a camera. Image pairs are recorded at a known time separation during which the tracers are displaced by the flow. The images are then divided into interrogation windows, e.g. with a size of 16 × 16 px. The tracers' displacement within each window is determined using cross-correlation. By dividing the measured displacement by the time separation, one velocity vector for each window is obtained. This technique has been also used to measure velocity fields in multi-phase flows, such as particle laden flows. Hoseini et al. (2015) separated fibers and flow tracer particles in image pre-processing and reconstructed the flow field with CC-PIV on images containing only the tracers. They studied the effect of fiber length on the difference between fiber and flow velocity in wall turbulence. Capone et al. (2021) took a similar measurement and processing approach and investigated the effect of the aspect ratio of fibers on

* Corresponding author.
*E-mail address:* alfredo.soldati@tuwien.ac.at (A. Soldati).

https://doi.org/10.1016/j.ijmultiphaseflow.2024.105021
Received 26 July 2024; Received in revised form 26 September 2024; Accepted 6 October 2024
Available online 15 October 2024

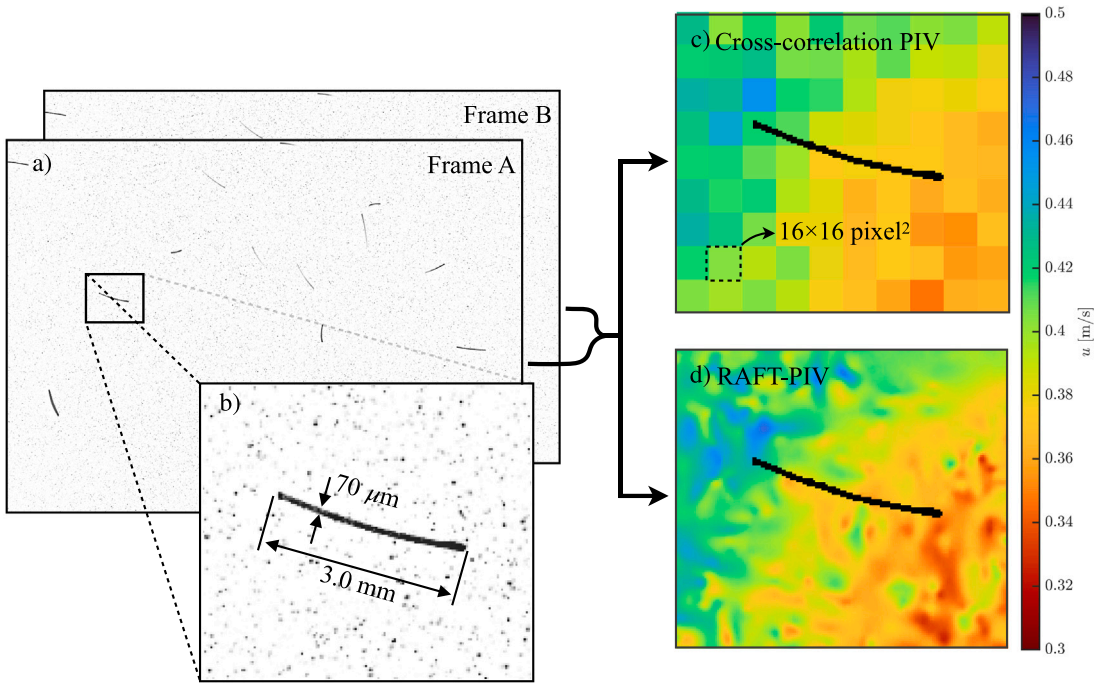


**Fig. 1.** Flowchart of the present investigation: panel (a) two raw images separated in time by 0.68 ms, panel (b) close-up of spherical tracers and a fiber, and panel (c) and (d) streawise velocity fields computed with cross-correlation-based PIV and a machine learning model - RAFT-PIV, respectively.

flow velocity moments up to the third order in a turbulent channel flow. Baker and Coletti (2022) studied inertial spheres, disks, and fibers with a Stokes number of $\mathcal{O}(10)$ in a turbulent boundary layer and took a similar processing approach. In their study, they measured the local slip velocity between the particles and the flow, omitting to report and discuss correlations between fiber rotation rates and flow quantities. The spatial resolution of their velocity fields was 8 px, due to their interrogation window size of 32 px and 75% overlap between windows. The limits of the spatial resolution of classical PIV have been overcome with a new method called *single-pixel ensemble correlation* (Westerweel et al., 2004), which achieves single-pixel resolution by averaging the spatial cross-correlation over multiple image pairs. This technique, however, can be almost exclusively used in (quasi-) stationary or periodic flows and provides only mean velocity fields, making it unsuitable for measurements of time-resolved, local, turbulent flow-fields around particles.

In contrast, time-resolved velocity vector fields at single-pixel resolution may be obtained from time-separated particle images with optical flow techniques, which estimate the two-dimensional displacement field of patterns between successive images. These include classical methods such as Horn-Schunck (Horn and Schunck, 1981) and Lucas-Kanade (Lucas and Kanade, 1981), physics-based approaches such as Liu-Shen (Liu and Shen, 2008), and hybrid methods enhancing the resolution of cross-correlation PIV (Seong et al., 2019). Liu et al. (2015) investigated the effect of particle displacement, velocity gradient, and particle image diameter and density on the accuracy of a Horn-Schunck optical flow method combined with a Liu-Shen estimator. Mendes et al. (2022) benchmarked combined optical flow methods against cross-correlation PIV on synthetic images generated from simple planar flows. They found the high-performance range of the former broader than correlation-based PIV. The authors underlined the necessity to study their performance in turbulent flows and compare them to machine learning approaches. Cai et al. (2019) benchmarked an optical flow method based on the Horn-Schunck algorithm and found it of higher accuracy than both a cross-correlation PIV and their proposed machine learning approach, PIV-LiteFlowNet-en, on synthetic images generated from a direct numerical simulation of a turbulent channel flow.

A recent alternative is represented by machine learning techniques which have demonstrated to achieve single-pixel resolution in time-resolved velocity fields. Specifically, Lagemann et al. (2021b) introduced a deep neural network-based approach called RAFT-PIV (Recurrent All-Pairs Field Transforms - Particle Image Velocimetry), based on an optical flow architecture (Teed and Deng, 2020). This approach is robust to common error sources, such as large displacements and their gradients, seeding density, and peak-locking. Moreover, it matches at least the accuracy of cross-correlation based PIV methods and even resolves shorter displacement wave-lengths without requiring third-order B-spline interpolation of sparse velocity fields onto single-pixel grids (Lagemann et al., 2022a). RAFT-PIV was found to estimate the displacement fields from a direct numerical simulation of a turbulent channel flow with an error about 7 times lower than the Horn-Schunck optical flow algorithm (Lagemann et al., 2021b).

Therefore, this study exploits the single-pixel resolution and accuracy of RAFT-PIV to measure the local time-resolved flow-field surrounding fibers in a turbulent channel flow, aiming at correlating the fiber rotation rates with vortical coherent flow structures. Fig. 1 shows the flow-chart of the present investigation. Panel (a) shows two images, frame A and B, of spherical flow tracers and fibers which are recorded with a set time separation. A close-up view of a 3 mm long and 70 μm thick fiber is shown in panel (b). Classic, cross-correlation PIV uses the tracers to resolve the flow-field around the fiber at 16 px spatial resolution, which is shown in panel (c). Using RAFT-PIV, the flow-field around the fiber is resolved with single-pixel resolution and is shown in panel (d). The manuscript is organized as follows: Section 2 describes the TU Wien Turbulent Water Channel facility, imaging setup, experimental conditions, seeding and fiber characteristics, image processing approach, and the machine learning technique used: RAFT-PIV; Section 3 compares an instantaneous streamwise velocity field obtained with cross-correlation PIV and RAFT-PIV and reports the mean streamwise velocity profiles and Reynolds stress, shows the streamwise and wall-normal slip velocity and swirling strength around a fiber trajectory, characterizes a hairpin vortex overlapping it, and shows the probability density function of fiber rotation rates conditioned on the presence or absence of a vortical structure; and Section 4 draws the conclusions.

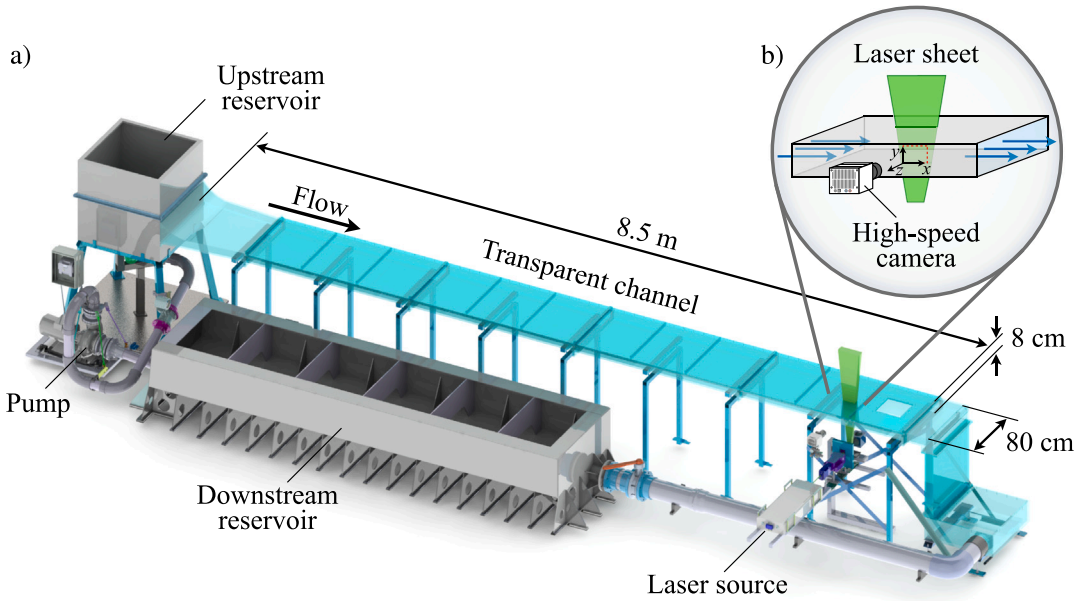


**Fig. 2.** Schematic of the TU Wien Turbulent Water Channel: (a) flow loop consisting of two reservoirs at atmospheric pressure, a centrifugal pump, a transparent channel, and a test-section with a high-speed laser and camera. (b) close-up view of the planar imaging setup.

## 2. Methodology

The experiments are conducted in the TU Wien Turbulent Water Channel, a facility designed to study particle dynamics in turbulent wall-bounded flows (Giurgiu et al., 2023). Fig. 2 shows a sketch of the facility. Water is recirculated from the downstream reservoir having a capacity of 3000 L to the upstream reservoir by a centrifugal volute pump, capable of a maximum flow rate of $175\,\mathrm{m^3\,h^{-1}}$, generating a maximum Shear Reynolds number of 1580. Precise and repeatable experiments are enabled through the control system of the hydraulic circuit which maintains a Shear Reynolds number constant within ±1% by monitoring the flow rate and temperature and adjusting the pump voltage in real-time (Giurgiu et al., 2023). The flow is subsequently driven by gravity through the channel with an inner height $2h = 80\,\mathrm{mm}$ and width $w = 800\,\mathrm{mm}$, dimensions which ensure negligible side-wall influence on center-span measurements. The test section is located 8.5 m downstream from the inlet, where the statistical properties of the turbulent flow field are comparable to direct numerical simulations (DNS) of stream-wise periodic channels (Giurgiu et al., 2023). The transparent channel allows optical access for imaging techniques such as Particle Image Velocimetry and Particle Tracking Velocimetry (PTV).

The present experiments are performed at a temperature of 24.1 °C and a Shear Reynolds number $Re_\tau = u_\tau h/\nu = 1000$, where $u_\tau = 22.8\,\mathrm{mm\,s^{-1}}$, and $\nu = 0.91\,\mathrm{mm^2\,s^{-1}}$ (e. V., 2013) are the friction velocity, and kinematic viscosity, respectively. In these conditions, the viscous length scale is $\delta_\nu = h/Re_\tau = 40\,\mu\mathrm{m}$ and viscous time scale is $\tau = \nu/u_\tau^2 = 1.76\,\mathrm{ms}$.

The imaging and illumination system is composed of a high-speed Phantom VEO 340L camera equipped with 100 mm Tokina AT-X Pro Macro optics, a Litron LD25-527 PIV laser, and optical lenses expanding the laser beam. The camera observes perpendicular to the side-wall the laser illuminated plane, which is normal to the bottom wall and aligned with the stream-wise direction. The acquisition frequency is 1478 Hz and the optical magnification is 35.25 px/mm. The images are 1792 × 1152 px large, resulting in a field of view of $50.8 \times 32.7\,\mathrm{mm^2}$ in the stream-wise $x$ and wall-normal $y$ directions, respectively. Spherical Polyamide particles with a diameter of $d_s = 20\,\mu\mathrm{m}$ and a density of $\rho_s = 1150\,\mathrm{kg\,m^{-3}}$ are used for seeding. The particle image density is 0.03 particles-per-pixel. With respect to the viscous time, their translational Stokes number is $St_s^+ = \rho_s d_s^2/(18\nu\rho)/\tau = 0.016$, with a water density of $\rho = 997.3\,\mathrm{kg\,m^{-3}}$ (e. V., 2013). The dispersed phase in the flow consists of Polyamide fibers with a density of $\rho_f = 1150\,\mathrm{kg\,m^{-3}}$, diameter of $d_f = 70\,\mu\mathrm{m}$, and length of $l_f = 3\,\mathrm{mm}$. Their aspect ratio is $\lambda = l_f/d_f = 43$. In these flow conditions, their Stokes number is (Bernstein and Shapiro, 1994):

$$St_f^+ = \frac{\rho_f d_f^2}{18\nu\rho}\frac{\lambda \ln\left(\lambda + \sqrt{\lambda^2-1}\right)}{\sqrt{\lambda^2-1}}\frac{1}{\tau} = 0.87\ .$$

The raw images captured by the camera are pre-processed to reduce background noise, improving the contrast of tracers and fibers. A raw and a pre-processed image of a fiber and tracers around it are shown in Fig. 3(a) and (b). The later has been produced by subtracting the minimum light intensity in each pixel within 13 frames to avoid imaging static optical defects. A sliding minimum in a window of 7 × 7 px is subtracted from each pixel to reduce the fiber image diameter. Finally, the image is normalized with the local average over all frames within a window of 500 × 500 px. The pre-processed image is binarized with a threshold of 20% of the maximum light intensity. Fibers are identified as connected regions of pixels with a length above 50 px and are subtracted to obtain the tracer images shown in Fig. 3(c). These are used to extract the flow velocities around the fiber with RAFT-PIV. The fiber image shown in Fig. 3(d) is used for fiber tracking with a nearest-neighbor approach using a 30 px search radius between time-steps. Built fiber trajectories contain the center-of-mass positions and fiber orientation, which is defined as the angle between the streamwise direction and the eigenvector corresponding to the highest eigenvalue of the inertia tensor of the fiber image. Positions and orientation angles are filtered with a Robust Locally Weighted Scatterplot Smoothing ('rlowess') (Cleveland, 1979) filter with a kernel of $4\tau$. The temporal derivative of the fibers' center-of-mass positions and of orientation angles are approximated with a 5-point stencil finite difference scheme to obtain translational and rotational velocities.

Images containing only the spherical tracers are used to obtain the flow velocity fields with the software PaIRS-UniNa 0.1.11. (Astarita and Cardone, 2005; Astarita, 2007, 2009) for comparison. A multi-pass approach has been used, with a final interrogation window of 32 × 32 px which together with a 50% overlap has yielded velocity fields at 16px resolution, corresponding to a vector pitch of 0.45 mm. The chosen final interrogation size ensures at least 8 tracer images within. At the chosen

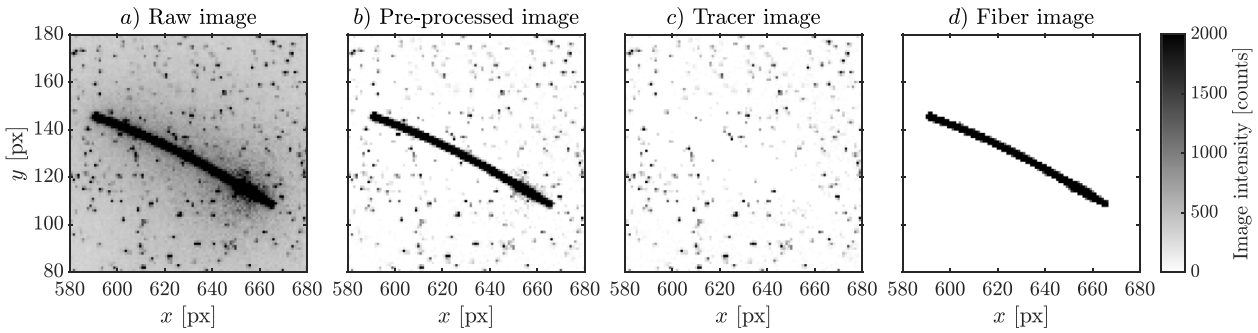


**Fig. 3.** Raw image of a fiber with tracers (a) and pre-processed image (b). The images containing only the tracers and only the fiber are shown in panels (c) and (d), respectively.

acquisition frequency the most-probable stream-wise displacement is 10 px/frame.

RAFT-PIV is a recently introduced deep optical flow network (Lagemann et al., 2021b) which is specifically designed for the use case of PIV images and loosely inspired by the famous RAFT architecture (Teed and Deng, 2020). In a variety of test applications ranging from standard turbulent boundary layer and channel flows (Lagemann et al., 2023) to more challenging transonic airfoil buffet measurements (Lagemann et al., 2022b, 2024c), blood flow investigations in the human cardio-vascular tract (Lagemann et al., 2024b), and the analysis of highly turbulent flow in internal combustion engines (Lagemann et al., 2022a), it has shown a new level of output resolution accuracy. Moreover, it enables a precise analysis of small-scale flow features and near-wall quantities, e.g., friction velocity and the wall-shear stress, which are typically challenging to measure from standard PIV experiments using established cross-correlation based processing methods. Here, it is noteworthy that these quantities can be analyzed in a spatially and temporally resolved fashion without applying any further modeling assumption or interpolation as typically required by other methods making it an valuable PIV processing method for the analysis of the present multiphase flow.

RAFT-PIV requires a graphical-processing-unit (GPU) with a large video memory compared to cross-correlation PIV, which usually runs on a central-processing-unit (CPU) with low memory requirements. For comparison, CC-PIV processed an image pair with a size of $1792 \times 1152$ px obtaining $111 \times 71$ vectors in about 2 s on an Intel Core i9-12900K CPU. In contrast, RAFT-PIV computes displacement fields at a 16 times higher spatial resolution, i.e. $1792 \times 1152$ vectors, but requires for a single particle image pair approximately 2 min on a standard NVIDIA RTX 3060 16 GB GPU. However, using more powerful GPUs, e.g. NVIDIA A100 GPUs which have been used in the present study, can reduce the compute time to approximately 20 s.

Overall, RAFT-PIV is designed to learn the mapping from input particle image pairs to the corresponding displacement fields. During training, the network minimizes a loss function that quantifies the discrepancy between the predicted and the ground-truth displacement, generated with, for example, a DNS of a turbulent channel flow (Lee and Moser, 2015). The general architecture of RAFT-PIV consists of the following stages: a feature and a context extracting block, the computation of a pixelwise correlation volume using an all-pairs correlation, and iterative updates based on a ConvGRU as shown in Fig. 4. In particular, the shared feature encoder computes high-dimensional latent representations $\boldsymbol{E_1}$, $\boldsymbol{E_2}$ of size $(M \times N \times D)$ for each input image individually using three convolutional neural network modules. These encoding steps transform the input particle images into a dense feature representation with $D$ dimensions. Broadly speaking, each channel of these high-dimensional feature maps contains an extract of the most relevant image patterns like edges or simple textures which become more complex patterns with increasing network depth. The context encoder leverages the same architecture as the feature encoder, but is only applied to the first particle image to derive anchoring context features for later network stages.

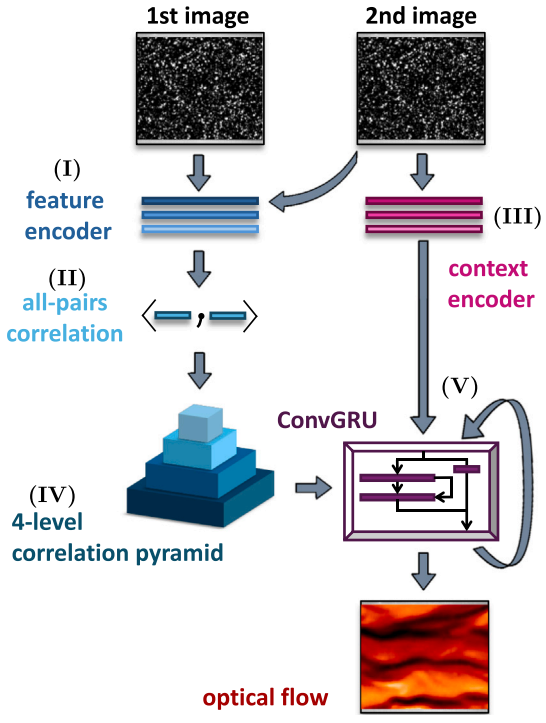


**Fig. 4.** Main components of RAFT-PIV comprising a shared feature encoder (I), the context encoder using the same topology as the feature encoder (III), an All-Pairs correlation layer (II), a correlation pyramid (IV), and the update operator (V) which recurrently updates the optical flow estimates using a convolutional GRU.

During the second stage, the similarity of both image feature representations $\boldsymbol{E}_1$ and $\boldsymbol{E}_2$ is computed using a full correlation volume between all pairs of both feature maps. Mathematically, the similarity between two pixel embeddings $(\mathbf{E}_{i,j}, \mathbf{E}_{k,l})$ is measured by the dot product between two individual feature vectors

$$\boldsymbol{C}_{ijkl} = \sum_{d=1}^{D} (\boldsymbol{E}_1)_{ijd} \cdot (\boldsymbol{E}_2)_{kld} \tag{1}$$

with $i, j$ denoting pixel coordinates in the image embedding $\boldsymbol{E}_1$ and $k, l$ in $\boldsymbol{E}_2$. In this context, all-pair correlation indicates that every pixel is correlated with every other pixel. Hence, $\boldsymbol{C}(i, j, :, :)$ represents a similarity map of pixel $(i, j)$ in $\boldsymbol{E}_1$ with all pixels of the second image $\boldsymbol{E}_2$. Afterwards, a 4-layer correlation pyramid is formed (see Fig. 4) pooling the last two dimensions of $\boldsymbol{C}$ sequentially from level to level (equivalent to kernel strides of $1, 2, 4, 8$).

Please note that this correlation pyramid is pre-computed once, and during the update process, only small neighborhoods around specific target locations are extracted. For clarification, let us suppose we have

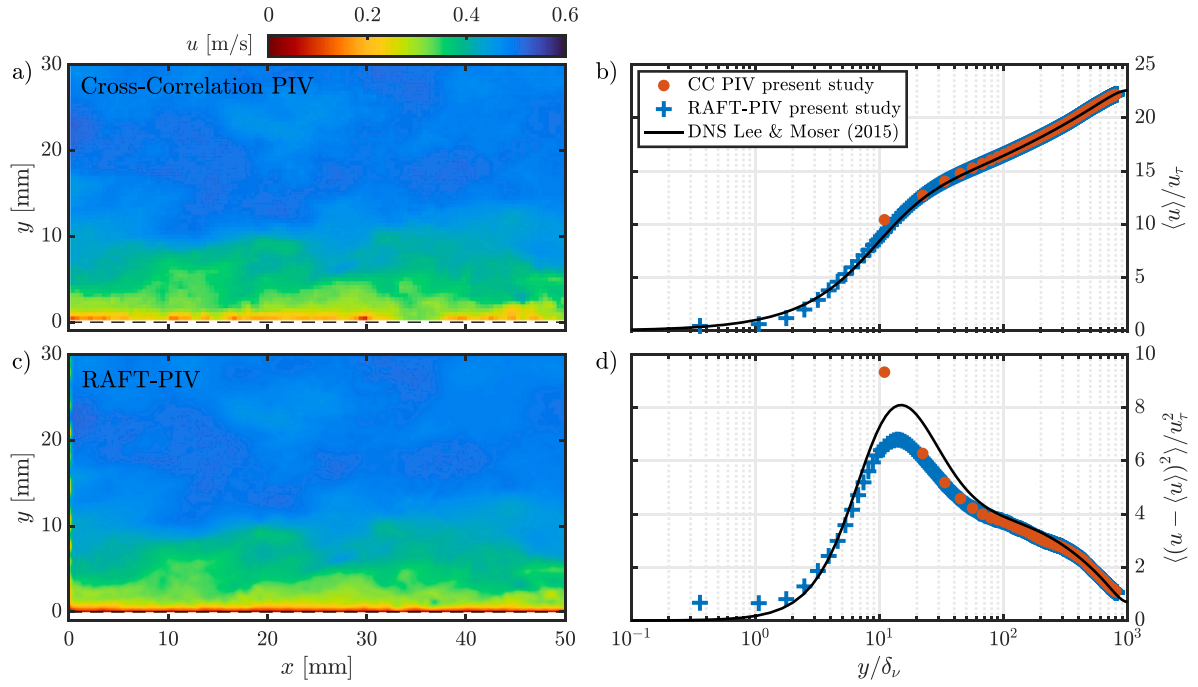


**Fig. 5.** Contour of an instantaneous streamwise velocity field measured with cross-correlation PIV (a) and RAFT-PIV (c). The wall is highlighted by the black dashed line. Panels (b) and (d) show the mean streamwise velocity and Reynolds stress profiles, respectively, computed using cross-correlation PIV, RAFT-PIV, and DNS (Lee and Moser, 2015) at $Re_\tau = 1000$.

the optical flow for the $i$th update step and we want to associate each pixel in $\boldsymbol{E}_1$ with its estimated location in $\boldsymbol{E}_2$. To determine the valid index for the correlation volume, an index operation is applied across all levels of the correlation pyramid which extracts a small neighborhood around the estimated location in $\boldsymbol{E}_2$. The intuition behind this complex operation can be formulated as follows: for a specific target location $(i, j)$ in encoding $\boldsymbol{E}_1$, the corresponding value in the correlation volume expresses the similarity of a pixel embedding at position $(k, l)$ in encoding $\boldsymbol{E}_2$ and its level-specific neighborhood. Consequently, this means that the higher the pyramid level of the extracted patch, the more spatial information of the original image features is covered, but the coarser the resolution of the correlation information becomes. Leveraging this multi-scale approach, RAFT-PIV can effectively handle large displacements of small particles. The final output is then a concatenation of the extracts of every pyramid level which forms the so-called motion feature.

It is subsequently decoded in the ConvGRU (Siam et al., 2017) to obtain a new optical flow update. This recurrent neural network maintains hidden state information from previous time steps to modulate a limited content memory. In simpler words, by considering observations from earlier steps, it estimates future predictions. The key difference between a ConvGRU and a standard recurrent neural network lies in the presence of update and reset gates. When applied in our work, the ConvGRU takes previous flow data, updated correlation information, and the context representation as input. It then produces a new hidden state, denoted as $\mathbf{h}_t$. This $\mathbf{h}_t$ is subsequently passed through two convolutional layers, resulting in the flow update $\boldsymbol{\Delta V}$. Hence, the final flow prediction emerges as a combination of residual flow updates and balances predictions based on earlier optical flow estimates and the current hidden state. The final output of the ConvGRU, i.e., the optical flow update, is a high-resolution velocity field at the original image resolution.

The original RAFT-PIV architecture was trained on a purely synthetic dataset in a supervised fashion. However, due substantially varying particle image conditions in the present experimental setup, a distribution shift between the datasets of training and inference phase was observed. Therefore, we augmented the training pipeline by a self-supervised training phase as outlined in Lagemann et al. (2024a) to fine-tune our initial network weights in the present measurement conditions. The loss objectives of this unsupervised learning step are purely based on geometric penalty terms and, hence, no ground truth is required. In line with Lagemann et al. (2021a) and Lagemann and Schröder (2023), the applied loss objective comprises the generalized Charbonnier loss to penalize photometric differences between source and warped target image, an adaptive loss objective to address forward/backward flow inconsistencies, an adaptive second-order smoothness objective, and an adaptive robust loss entity which regularizes differences between the teacher and student predictions. As a consequence, the RAFT-PIV network can be fine-tuned directly on our experimental measurement data which reduces drastically the occurrence of outliers and spurious vectors. A reference implementation of RAFT-PIV is available as an open-source tool and can be accessed at https://github.com/cl126162/WSSflow.

## 3. Results

The same pair of two consecutive tracer images are processed with PaIRS-UniNa (CC-PIV) and RAFT-PIV to obtain the instantaneous streamwise velocity fields shown in Fig. 5(a) and (c), respectively. Both are spatially filtered with a Gaussian kernel of 41 px and temporally with a 'rlowess' (Cleveland, 1979) filter with a kernel of $4\tau$. They exhibit the same general large-scale features, however the field obtained with RAFT-PIV has a 16 times higher spatial resolution, both in the horizontal and vertical directions, resulting in 256 times more velocity vectors, feature which is exploited in this study to resolve the flow field around the fibers. Moreover, this also allows the flow field measurement closer to the wall, which is shown in panels (a) and (c) with a dashed line at $y = 0\,\text{mm}$. The left (inlet) part of the RAFT-PIV field exhibits outliers, which are typical for optical flow methods due to occlusions at image boundaries. In the computation of the following results, this region of 16 px has been disregarded. Panel (b) compares as a function of the wall-normal direction, the mean streamwise velocity measured with CC-PIV and RAFT-PIV and computed with DNS (Lee

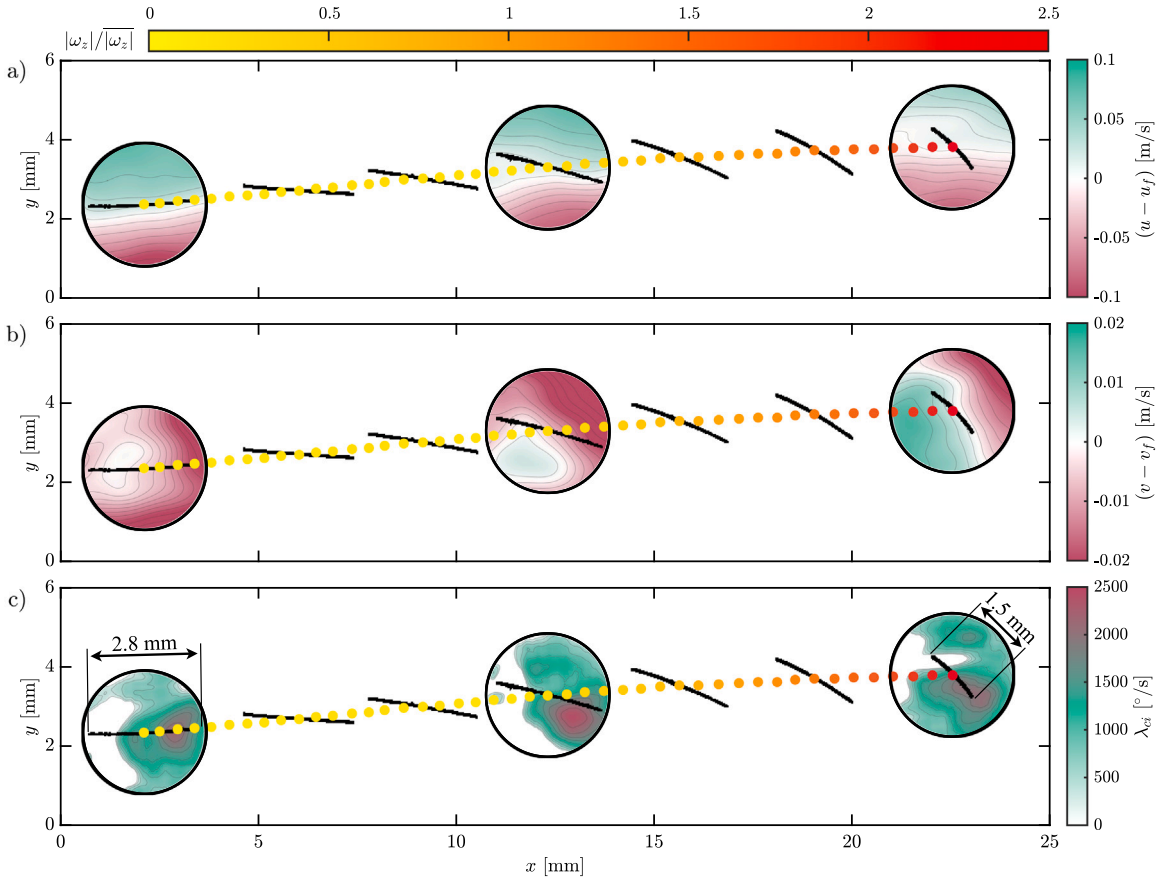


**Fig. 6.** An example of a fiber trajectory interacting with a hairpin vortex. The instantaneous orientation of the fiber is coupled with the contour maps of the two components of the slip velocity ($u-u_f$ in (a), $v-v_f$ in (b)) and the swirling strength, $\lambda_{ci}$ (c). Overlain dots indicate the center of mass of the fiber along its trajectory and their color represents the spanwise rotation rate normalized by the mean track rotation rate, $\overline{|\omega_z|} = 815°\ s^{-1}$.

and Moser, 2015) at the same $Re_\tau = 1000$. Across the whole channel half-height, an excellent agreement is found between the three profiles. However, the profile obtained with CC-PIV starts at $11y/\delta_v$ away from the wall. RAFT-PIV provides 7 measurement points within the viscous sub-layer ($y/\delta_v < 5$), the first one located at $0.35y/\delta_v$, which corresponds to 14 µm and is equivalent to 0.5 px. Measurements in the viscous sub-layer enable the quantification of the wall-shear stress (Lagemann et al., 2024b), which can be used to conduct drag-reduction studies with different fiber concentrations. Panel (d) shows the streamwise Reynolds stress over the wall-normal direction computed with cross-correlation PIV, RAFT-PIV, and DNS (Lee and Moser, 2015). A good agreement is observed between the three profiles at wall-normal locations above $\approx 80y/\delta_v$. The CC-PIV and RAFT-PIV profiles overlap above $20y/\delta_v$. The CC-PIV profile fails to predict a peak in the Reynolds stress with the point at $11y/\delta_v$ overestimating the DNS. RAFT-PIV shows a clear peak, however shifted to a slightly lower wall-normal distance and reduced by 10% with respect to DNS. The attenuation of fluctuations between 8 and $80y/\delta_v$ is present both in CC-PIV and RAFT-PIV and might be explained by the large laser sheet thickness of about 3 mm used to obtain long fiber trajectories. The RAFT-PIV profiles shows an excellent agreement with DNS above 2 and below $8y/\delta_v$. Note that, in general, RAFT-PIV displays higher errors than CC-PIV in streamwise mean velocity and Reynolds stress at signal-to-noise (SNR) ratios, defined as the ratio between the maximum particle intensity and the background intensity, below 2 (Lagemann et al., 2022a). However, the images used in this study before background noise subtraction had an SNR of 13.

A fiber trajectory with a duration of $35\tau$ and the surrounding flow field obtained with RAFT-PIV are shown in Fig. 6. The flow field in panel (a) is shown in terms of streamwise slip velocity, i.e., the difference between the flow velocity and the velocity of the fiber's center of mass, $u-u_f$. The positions of the fiber's center of mass are shown as circles colored by the absolute fiber rotation rate normalized by its track mean, $|\omega_z|/\overline{|\omega_z|}$. Initially, the fiber is almost aligned parallel to the zero streamwise slip velocity isoline. This implies that no torque can be applied by the streamwise slip velocity distribution along the fiber. However, the fiber starts rotating clock-wise due to the torque applied by the wall-normal slip velocity, $v-v_f$, distribution along the fiber, which is shown in panel (b). The fluid around the left part of the fiber is moving upwards and around the right part downwards relative to the fiber's center of mass. The difference between the upward and downward flow velocity is $\mathcal{O}(0.01\,\mathrm{m\,s^{-1}})$. The resulting reorientation of the fiber increases the differences in streamwise slip velocity along its length, which are of $\mathcal{O}(0.1\,\mathrm{m\,s^{-1}})$, enabling a higher torque. In consequence, the fiber rotation rate increases, reaching up to $2.5\overline{|\omega_z|}$ in the last instance. Finally, Fig. 6(c) shows the swirling strength, $\lambda_{ci}$, around the fiber at the same three instances as previous panels. The swirling strength, $\lambda_{ci}$, is used to identify vortical flow structures and is the imaginary part of the complex eigenvalue of the velocity gradient tensor (Zhou et al., 1999):

$$\nabla \mathbf{u} = \begin{bmatrix} \frac{\partial u}{\partial x} & \frac{\partial u}{\partial y} \\ \frac{\partial v}{\partial x} & \frac{\partial v}{\partial y} \end{bmatrix},$$

which is approximated by a finite difference central scheme. During the whole trajectory, a vortex with a size of about half the fiber length overlaps the fiber. The projected image of the fiber in the first time-step is 2.8 mm long suggesting the fiber, having a nominal length of 3 mm, being almost parallel to the $x$–$y$ plane. However, during its trajectory, the fiber becomes increasingly more aligned with the

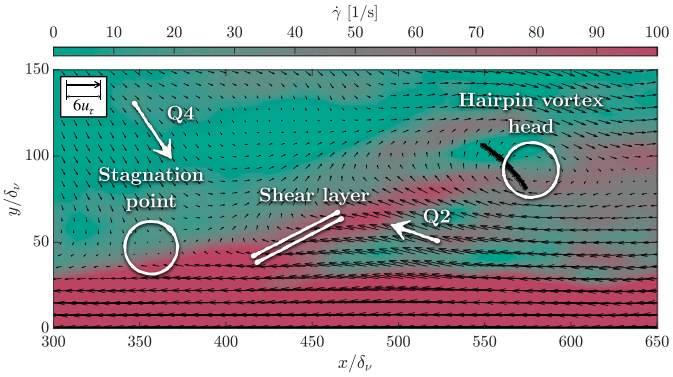


**Fig. 7.** Contour of the shear strain rate, $\dot{\gamma}$, measured with RAFT-PIV around the fiber from Fig. 6 at the last time instance. The colorbar saturates at $100\,s^{-1}$ for visualization purposes. Overlain black vectors indicate the flow velocity field after subtracting $16.1u_\tau$ from the streamwise velocity. Only every tenth vector is shown. The top left inset indicates the scale of the velocity vectors. White text and sketched arrows, lines, and circles indicate the signature components of a hairpin vortex: compact head, an ejection (Q2) and a sweep (Q4) event, an inclined shear layer, and a stagnation point (Adrian, 2007).

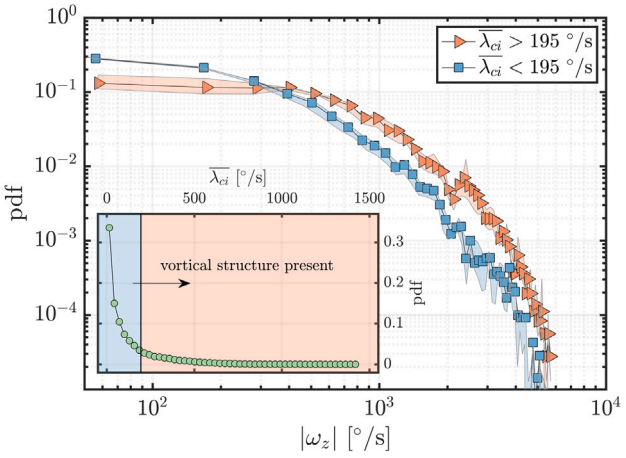


**Fig. 8.** Main panel: pdf of the fiber rotation rate conditioned on the presence of a vortex. The shaded regions indicate resulting variations when changing the vortex identification threshold by ±60%. Inset: pdf of swirling strength obtained with RAFT-PIV and averaged inside a circle (radius of 1.4 mm) centered around the fibers' center of mass. The threshold for vortex identification is shown by the vertical black line.

$z$ direction, evident from the reduction of the projected fiber image to 1.5 mm in the last instance. To determine whether the increasing spanwise fiber orientation implies an alignment with the axis of the vortical structure identified through $\lambda_{ci}$, the vortex must be first characterized. This is essential because, in Fig. 6c, only the projection of the vortex is available, which does not directly imply that the axis of the vortex is oriented spanwise. To this aim, Fig. 7 shows the shear strain rate, $\dot{\gamma} = \partial u/\partial y + \partial v/\partial x$ (Kundu et al., 2015) around the fiber shown in Fig. 6 at the last time instance of its trajectory. A strong shear is measured below $30y/\delta_\nu$ due to the presence of the wall. More importantly, an inclined shear layer is observed. Moreover, overlain vectors quantify the velocity field after subtracting a streamwise velocity of $16.1u_\tau$. This allows the identification of a compact rotational region close to the fiber, a strong ejection event (Q2) and a weaker sweep event (Q4) which generate a stagnation point and the previously observed inclined shear layer. These are the signature components of a hairpin vortex (Adrian, 2007), a temporally and spatially coherent structure typical of wall-bounded turbulent flows most common in the logarithmic layer. It is an omega-shaped vortex with a compact head with its axis oriented spanwise and quasi-streamwise oriented legs. The head of the structure identified in Fig. 7 is located $100\delta_\nu$ away from the wall, which is the typical height of a hairpin vortex head (Adrian, 2007). Moreover, its streamwise length is about $200\delta_\nu$ from the beginning of the inclined shear layer to the head, which is also typical for hairpin vortices (Adrian, 2007). This evidence suggests, that the axis of the vortex near the fiber identified in Fig. 6c is indeed oriented spanwise, because it is the head of a hairpin vortex. This implies that the fiber shown in Fig. 6 starts perpendicular to the head of hairpin vortex and increasingly aligns its axis with the one of the vortex during its trajectory lasting $35\tau$. These findings are consistent with previous studies which also observed an alignment of fibers with vortical structures in homogeneous isotropic turbulence (Picardo et al., 2020; Ni et al., 2014, 2015) - DNS and experiments - and in turbulent channel flow at $Re_\tau = 180$ (Cui et al., 2021) - DNS.

The increase in fiber rotation rates with increasing alignment of the fiber principal axis with a vortical structure, demonstrated by one fiber trajectory shown in Fig. 6, warrants further study. To this aim, the effect of the presence of a vortex close to fibers on their rotation rate is investigated in Fig. 8. The presence of a vortical structure is identified by a threshold value on the mean swirling strength, $\overline{\lambda_{ci}}$, obtained as an average inside a circle with a radius of 1.4 mm and centered around the fibers' center of mass. The inset of Fig. 8 shows the probability density function (pdf) of $\overline{\lambda_{ci}}$. A vortex is considered present within the circle if the mean swirling strength exceeds the chosen value of $195°\,s^{-1}$. Note that $\overline{\lambda_{ci}}$ for the fiber at the three time instances in Fig. 6 is 814, 854, and $928°\,s^{-1}$. The main panel of Fig. 6 shows the pdf of the absolute fiber rotation rate with and without a detected vortex near the fiber. The lowest fiber rotation rates are more than twice as likely to occur if no vortical structure is present. Fiber rotation rates higher than $400\,°\,s^{-1}$ are likelier to occur when a vortex is present, which suggests a positive correlation between $\lambda_{ci}$ and $|\omega_z|$. The results in Fig. 8 have been obtained from about 2300 fiber trajectories totaling $2 \times 10^5$ data points.

## 4. Conclusions

Proper quantification of oceanic microplastic pollution requires accurate estimates of transport, sedimentation rates, and rotational dynamics of elongated microplastic fibers interacting with turbulent flows. This work demonstrated how RAFT-PIV, an open-source machine learning-based technique, can be used to measure the local time-resolved flow field around microplastic fibers in a turbulent channel flow at a Shear Reynolds of 1000. This approach produced flow fields with 16 times higher resolution, both in the horizontal and vertical directions, resulting in 256 times more velocity vectors than cross-correlation-based PIV. RAFT-PIV was able to reconstruct a hairpin vortex, a typical topological feature of wall-bounded turbulence, allowing the observation of the interaction of a fiber with this vortex. Statistical analysis showed that higher fiber rotation rates were more likely in the presence of a nearby vortical structure compared to when it was absent. In the future, an in-depth statistical analysis will help to generalize the observed behaviors and further validate the correlation between fiber rotation and vortical structures.

## CRediT authorship contribution statement

**Vlad Giurgiu:** Writing – review & editing, Writing – original draft, Visualization, Methodology, Investigation, Formal analysis, Data curation, Conceptualization, Software. **Leonel Beckedorff:** Visualization, Methodology, Conceptualization, Software, Formal analysis, Data curation, Writing – review & editing. **Giuseppe C.A. Caridi:** Writing – review & editing, Supervision, Visualization. **Christian Lagemann:** Software, Methodology, Resources, Writing – original draft, Writing – review & editing, Funding acquisition. **Alfredo Soldati:** Writing – review & editing, Supervision, Resources, Project administration, Funding acquisition.

## Declaration of competing interest

The authors declare that they have no known competing financial interests or personal relationships that could have appeared to influence the work reported in this paper.

## Acknowledgments

This research was funded in part by the Austrian Science Fund (FWF) (Grant No. 10.55776/P-35505) (V.G., L.B., G.C. & A.S.) and the German Research Foundation (LA 5508/1-1) (C.L.). Furthermore, the authors gratefully acknowledge the Gauss Centre for Supercomputing e.V. for funding this project by providing computing time on the GCS Supercomputers. Finally, the authors acknowledge TU Wien Bibliothek for financial support through its Open Access Funding Programme.

## Role of the funding source

This research was supported by the Austrian Science Fund (FWF) (Grant No. P-35505), the German Research Foundation (Grant No. LA 5508/1-1), and the TU Wien Bibliothek. The funding bodies had no role in the writing of the manuscript, data collection, analysis, interpretation, or decision to submit the manuscript for publication. The authors were not precluded from accessing the data in the study and take full responsibility for the decision to submit the manuscript for publication.

## Data availability

Data will be made available on request.

## References

Adrian, R.J., 2007. Hairpin vortex organization in wall turbulence. Phys. Fluids 19 (4).
Alipour, M., De Paoli, M., Ghaemi, S., Soldati, A., 2021. Long non-axisymmetric fibres in turbulent channel flow. J. Fluid Mech. 916.
Astarita, T., 2007. Analysis of weighting windows for image deformation methods in PIV. Exp. Fluids 43 (6), 859–872.
Astarita, T., 2009. Adaptive space resolution for PIV. Exp. Fluids 46 (6), 1115–1123.
Astarita, T., Cardone, G., 2005. Analysis of interpolation schemes for image deformation methods in PIV. Exp. Fluids 38 (2), 233–243.
Baker, L.J., Coletti, F., 2022. Experimental investigation of inertial fibres and disks in a turbulent boundary layer. J. Fluid Mech. 943, A27.
Bernstein, O., Shapiro, M., 1994. Direct determination of the orientation distribution function of cylindrical particles immersed in laminar and turbulent shear flows. J. Aerosol Sci. 25 (1), 113–136.
Cai, S., Liang, J., Gao, Q., Xu, C., Wei, R., 2019. Particle image velocimetry based on a deep learning motion estimator. IEEE Trans. Instrum. Meas. 69 (6), 3538–3554.
Capone, A., Di Felice, F., Alves Pereira, F., 2021. Flow-particle coupling in a channel flow laden with elongated particles: The role of aspect ratio. J. Mar. Sci. Eng. 9 (12), 1388.
Cleveland, W.S., 1979. Robust locally weighted regression and smoothing scatterplots. J. Amer. Statist. Assoc. 74 (368), 829–836.
Cui, Z., Huang, W.-X., Xu, C.-X., Andersson, H.I., Zhao, L., 2021. Alignment of slender fibers and thin disks induced by coherent structures of wall turbulence. Int. J. Multiph. Flow 145, 103837.
Giurgiu, V., Caridi, G.C.A., Alipour, M., De Paoli, M., Soldati, A., 2023. The TU Wien Turbulent Water Channel: Flow control loop and three-dimensional reconstruction of anisotropic particle dynamics. Rev. Sci. Instrum. 94 (9).
Giurgiu, V., Caridi, G.C.A., De Paoli, M., Soldati, A., 2024. Full rotational dynamics of plastic microfibers in turbulence. Phys. Rev. Lett. 133 (5), 054101.
Horn, B.K., Schunck, B.G., 1981. Determining optical flow. Artif. Intell. 17 (1–3), 185–203.
Hoseini, A.A., Lundell, F., Andersson, H.I., 2015. Finite-length effects on dynamical behavior of rod-like particles in wall-bounded turbulent flow. Int. J. Multiph. Flow 76, 13–21.
Kundu, P.K., Cohen, I.M., Dowling, D.R., 2015. Fluid Mechanics. Academic Press.
Lagemann, E., Brunton, S.L., Lagemann, C., 2024b. Uncovering wall-shear stress dynamics from neural-network enhanced fluid flow measurements. Proc. R. Soc. A 480 (2292), 20230798.
Lagemann, E., Brunton, S.L., Schröder, W., Lagemann, C., 2024c. Towards extending the aircraft flight envelope by mitigating transonic airfoil buffet. Nature Commun. 15 (1), 5020.
Lagemann, C., Klaas, M., Schröder, W., 2021a. Unsupervised recurrent all-pairs field transforms for particle image velocimetry. In: 14th International Symposium on Particle Image Velocimetry. Vol. 1.
Lagemann, C., Lagemann, K., Mukherjee, S., Schröder, W., 2021b. Deep recurrent optical flow learning for particle image velocimetry data. Nat. Mach. Intell. 3 (7), 641–651.
Lagemann, C., Lagemann, K., Mukherjee, S., Schröder, W., 2022a. Generalization of deep recurrent optical flow estimation for particle-image velocimetry data. Meas. Sci. Technol. 33 (9), 094003.
Lagemann, C., Lagemann, K., Mukherjee, S., Schröder, W., 2024a. Challenges of deep unsupervised optical flow estimation for particle-image velocimetry data. Exp. Fluids 65 (3), 30.
Lagemann, C., Mäteling, E., Klaas, M., Schröder, W., 2022b. Analysis of PIV images of transonic buffet flow by recurrent deep learning based optical flow prediction. In: 20th International Symposium on Applications of Laser and Imaging Techniques To Fluid Mechanics. Vol. 1.
Lagemann, C., Schröder, W., 2023. Key aspects of unsupervised optical flow models in PIV applications. In: 15th International Symposium on Particle Image Velocimetry. Vol. 1.
Lagemann, E., Schröder, W., Lagemann, C., 2023. Instantaneous wall-shear stress distribution based on wall-normal PIV measurements using deep optical flow. In: 15th International Symposium on Particle Image Velocimetry. Vol. 1.
Lee, M., Moser, R.D., 2015. Direct numerical simulation of turbulent channel flow up to Re 5200. J. Fluid Mech. 774, 395–415.
Liu, T., Merat, A., Makhmalbaf, M., Fajardo, C., Merati, P., 2015. Comparison between optical flow and cross-correlation methods for extraction of velocity fields from particle images. Exp. Fluids 56, 1–23.
Liu, T., Shen, L., 2008. Fluid flow and optical flow. J. Fluid Mech. 614, 253–291.
Lucas, B.D., Kanade, T., 1981. An iterative image registration technique with an application to stereo vision. In: IJCAI'81: 7th International Joint Conference on Artificial Intelligence. Vol. 2, pp. 674–679.
Mendes, L.P., Ricardo, A.M., Bernardino, A.J., Ferreira, R.M., 2022. A comparative study of optical flow methods for fluid mechanics. Exp. Fluids 63 (1), 7.
Ni, R., Kramel, S., Ouellette, N.T., Voth, G.A., 2015. Measurements of the coupling between the tumbling of rods and the velocity gradient tensor in turbulence. J. Fluid Mech. 766, 202–225.
Ni, R., Ouellette, N.T., Voth, G.A., 2014. Alignment of vorticity and rods with Lagrangian fluid stretching in turbulence. J. Fluid Mech. 743, R3.
Picardo, J.R., Singh, R., Ray, S.S., Vincenzi, D., 2020. Dynamics of a long chain in turbulent flows: impact of vortices. Phil. Trans. R. Soc. A 378 (2175), 20190405.
Seong, J.H., Song, M.S., Nunez, D., Manera, A., Kim, E.S., 2019. Velocity refinement of PIV using global optical flow. Exp. Fluids 60, 1–13.
Siam, M., Valipour, S., Jagersand, M., Ray, N., 2017. Convolutional gated recurrent networks for video segmentation. In: 2017 IEEE International Conference on Image Processing. ICIP, IEEE, pp. 3090–3094.
Teed, Z., Deng, J., 2020. RAFT: Recurrent all-pairs field transforms for optical flow. In: European Conference on Computer Vision. Springer, pp. 402–419.
e. V., V., 2013. VDI-Wärmeatlas, eleventh ed. Springer Vieweg, Berlin, Heidelberg.
Voth, G.A., Soldati, A., 2017. Anisotropic particles in turbulence. Annu. Rev. Fluid Mech. 49, 249–276.
Westerweel, J., Geelhoed, P., Lindken, R., 2004. Single-pixel resolution ensemble correlation for micro-PIV applications. Exp. Fluids 37 (3), 375–384.
Zhou, J., Adrian, R.J., Balachandar, S., Kendall, T., 1999. Mechanisms for generating coherent packets of hairpin vortices in channel flow. J. Fluid Mech. 387, 353–396.